Synergetic proton and Mg^{2+}/Ca^{2+} insertion boosting aqueous divalent ion batteries

Rui Zhou, Ke Fan, Zhen Hou, Qun Liu, Haitao Huang and Biao Zhang**

Department of Applied Physics & Research Institute for Smart Energy, The Hong Kong Polytechnic University, Hung Hom, Hong Kong, China.

ABSTRACT: Divalent ion batteries (Mg^{2+}, Ca^{2+}) are promising candidates for next-generation energy storage devices. However, divalent ions' large radius and high charge density commonly lead to sluggish diffusion kinetics, resulting in an inferior capacity and rate capability. Herein, using an organic anode, 3,4,9,10-perylenetetracarboxylic diimide, as the model system, we report incorporating proton insertion with the metal ion to boost the reaction kinetics in aqueous electrolyte, as revealed by the combined spectroscopic analysis and theoretical simulations. The co-storage strategy enables an attractive specific capacity of 110 mAh g^{-1} at 0.2 A g^{-1} and capacity retention of 80% at 2 A g^{-1}, compared to 60 mAh g^{-1} and 56% for single Mg^{2+} insertion in the Mg-ion battery. A similar phenomenon is observed in the Ca-ion system, thus allowing the stable cycling of 1.1 V-class aqueous Mg-/Ca-ion full cells for over 2000 cycles. This work suggests the great potential of building high-power and long-lifespan aqueous divalent ion batteries enabled by the proton-assisted storage behavior.

Keywords: Proton co-insertion, Increased capacity, Fast kinetics, Aqueous electrolyte, Divalent ion batteries

1. Introduction

Owing to the merits of natural abundance and potentially high energy arising from two electron exchanges per ion, divalent magnesium and calcium-ion batteries (MIBs and CIBs) are considered as promising complements to Li-ion batteries.[1-5] Nevertheless, the development of MIBs and CIBs in organic electrolyte has been severely restricted by the poor kinetics at the interphases consisting mainly of the electrolyte decomposition products.[3, 6, 7] This challenge could be readily bypassed in aqueous electrolyte, which also brings about the benefits of low-cost, high safety and sustainability.[2, 8-10] To compensate the energy sacrifice arising from the narrow electrochemical window of aqueous electrolyte, high-capacity electrodes are being rigorously explored.

Several types of cathode materials have been investigated for aqueous MIBs and CIBs, such as Prussian blue analogues,[11-14] Mg_2MnO_4,[15-18] $MgFe_xMn_{2-x}O_4$,[19] Mg/Ca-birnessite,[20, 21] polyanion species ($Mg_xLiV_2(PO_4)_3$[22]) and metallic oxides (MnO_2[23-25], V_2O_5[10, 26]). Progresses have also been made in the development of anode materials.[27] For example, conversion materials (S[28], Se[29]) and $FeVO_4 \cdot nH_2O$[30, 31] have been reported recently but deliver insufficient electrochemical performance due to Mg^{2+}/Ca^{2+} sluggish diffusion and accelerated structural deterioration. Compared with the above inorganic electrodes, organic materials with highly flexible frameworks and unique ion coordination reactions show advantages in maintaining structural integrity.[32-39] Therefore, carbonyl and imine

organic compounds have been reported in MIBs and CIBs, delivering competitive electrochemical performance.[40-43]

It is worth noting that protons (H^+) could also serve as charge carriers in the aqueous system, as demonstrated in Zn-ion batteries.[33, 44-47] Benefiting from the Grotthuss conduction mechanism, H^+ can move rapidly in aqueous electrolyte through the formation/breakage of the hydrogen bond.[9, 48-50] Furthermore, proton insertion has been observed in the CIB system with extraordinary stability.[37] Nevertheless, since the H^+ insertion may compete with the Mg^{2+}/Ca^{2+}, whether H^+ charge carrier brings about a positive or negative impact on the cyclic stability and rate capability of MIBs and CIBs remains unclear. Recently, a π-π aromatic stacking organic compound, 3,4,9,10-perylenetetracarboxylic diimide (PTCDI) has been reported in divalent ion batteries.[51-54] We note that it shows a distinct electrochemical behavior in the organic and aqueous electrolytes, due possibly to the presence of H^+ in the latter. Therefore, we adopt the PTCDI as a model electrode in this work to explore the H^+ insertion behavior and its effect on the capacity and stability of Mg^{2+} and Ca^{2+} storage. Delightedly, we observe the simultaneous H^+ and Mg^{2+} insertion/extraction in aqueous electrolyte, leading to an increased specific capacity from 60 to 110 mAh g^{-1} and rate retention from 56% to 80% at a large current density of 2 A g^{-1}. Such an enhancement could be well extended to CIBs, providing a new avenue for boosting the energy of aqueous divalent ion batteries.

2. Experimental section

2.1 Materials and electrodes preparation

All chemicals involved in this manuscript were purchased and used as received without any further treatment. Commercial activated carbon (AC, YP80F) was purchased from Guangdong Canrd New Energy Technology Co., Ltd. A typical co-precipitation method was employed to synthesize copper hexacyanoferrate (CuHCF) particles. 20 ml of 0.1 M $Cu(NO_3)_2 \cdot 3H_2O$ (99%, Sigma-Aldrich) and 20 ml of 0.05 M $K_3Fe(CN)_6$ (99%, International Laboratory USA) were dropwise added into 60 ml deionized (DI) water under continuous stirring for 6 h at room temperature. The suspension was filtered, washed with DI water and ethanol several times, and dried for 24 h. The electrodes were prepared by mixing the active materials (PTCDI (95%, Macklin) or CuHCF powders), acetylene blacks (Guangdong Canrd New Energy Technology Co., Ltd.) and poly(1,1-difluoroethylene) (PVDF, DoDo Chem) at a mass ratio of 5:3:2 and 7:2:1 in N-methyl pyrrolidone (NMP, Guangdong Canrd New Energy Technology Co., Ltd.) to form homogenous slurries, which were cast onto stainless-steel and titanium foils, respectively. The electrodes were then dried at 80 ^oC under a vacuum. A freestanding PTCDI film was obtained after peeling from the stainless-steel foil. The magnesiated CuHCF (Mg_xCuHCF) was prepared in two steps. First, the CuHCF electrode was charged in 0.6 M K_2SO_4-H_2O electrolyte to extract K^+ and washed with DI water for several times. Subsequently, the electrode was electrochemically magnesiated in $Mg(TFSI)_2$-H_2O electrolyte to prepare the Mg_xCuHCF.

2.2 Characterizations

The morphologies of materials were obtained by scanning electron microscopy (SEM, TESCAN VEGA3). Fourier transform infrared spectroscopy (FTIR) spectra were collected with the Nicolet IS50 FTIR spectrometer to explore the chemical evolution of electrodes. X-ray photoelectron spectrometry (XPS) was carried out using a Thermo Scientific K-Alpha X-ray photoelectron spectrometer system. The solid-state ^{1}H nuclear magnetic resonance (NMR) was measured on a Bruker 600 MHz spectrometer (AVANCE NEO). Inductively coupled plasma optical emission spectroscopy (ICP-OES) analysis was conducted by Agilent 720 ES. Thermogravimetric analysis was conducted by Rigaku TG-DTA8122.

The electrochemical measurements and computational methods are provided in supporting information.

3. Results and discussion

3.1 Electrochemical behavior of PTCDI in non-aqueous and aqueous electrolytes

The electrochemical performance of PTCDI is first evaluated in organic and aqueous MIBs. Figure 1a presents the charge/discharge curves of PTCDI in 1 M $Mg(TFSI)_2$-EC/PC (ethylene carbonate/propylene carbonate with a volume ratio of 1:1) and H_2O electrolytes at 0.2 A g^{-1}. Owing to the poor reversibility of Mg plating/stripping in EC/PC-based electrolyte, AC is employed as the counter/reference electrode. The voltage of AC electrode is around 2.6 V and 2.9 V vs. Mg/Mg^{2+} in organic and aqueous electrolytes, respectively (Figure S1, S2).[55] In EC/PC-based electrolyte, PTCDI anode shows a sloping voltage profile with a specific capacity of 60 mAh g^{-1} and discharge average voltage of 2.0 V vs. Mg/Mg^{2+}, while a capacity of 110

mAh g^{-1} and 1.8 V average voltage are obtained in aqueous electrolyte. The low capacity in non-aqueous electrolyte originates from not only sluggish diffusion kinetics, but also the limited utilization of active groups induced by the spatial position restriction.[33, 56, 57] It is worth noting that PTCDI delivers distinct voltage profiles in two electrolytes. The non-aqueous one shows two plateaus, while the aqueous one presents four voltage plateaus, indicating a different ion storage mechanism in the two electrolytes, which is confirmed in the cyclic voltammetry (CV) curves (Figure S3). Besides, a superior rate performance is achieved in aqueous electrolyte. Specifically, the PTCDI anode delivers a capacity of 33 mAh g^{-1} at 2 A g^{-1}, corresponding to 56% of that at 0.2 A g^{-1} in non-aqueous electrolyte (Figure 1b). By contrast, it shows a much higher capacity retention of 80% under 2 A g^{-1} in aqueous electrolyte (Figure 1c). Even under a challenging current density of 10 A g^{-1}, it still sustains a decent discharge capacity of 65 mAh g^{-1} in 1 M $Mg(TFSI)_2$-H_2O electrolyte. After the current density restores to 0.2 A g^{-1}, PTCDI delivers a slightly higher capacity than that in initial state, which may be related to the improved electrolyte wettability into electrode after high-rate cycling.[58]

Such a tremendous disparity in the rate capability of PTCDI under different electrolytes may be attributed to the ionic diffusion kinetics. Galvanostatic intermittent titration technique (GITT) is employed to calculate the ionic diffusion coefficients along the electrode. The apparent diffusion coefficients along PTCDI electrode in aqueous system are about an order of magnitude higher than that in organic counterpart (Figure 1d, Figure S4 and S5).[59] We also examine the cyclic stability of PTCDI at a

current density of 1 A g^{-1} in these two electrolytes. A capacity increase process is observed in the initial hundred cycles in organic electrolyte. It may relate to the slow kinetics of Mg^{2+} insertion in PTCDI, requiring long activation cycles. On the contrary, such an activation process almost disappears in aqueous electrolyte. The low initial Coulombic efficiency in aqueous electrolyte is primarily attributed to side reactions such as hydrogen evolution reaction, which is suppressed in the subsequent cycles (Figure S6).[60, 61] Impressively, H_2O-based electrolyte enables a slight capacity decay after 1000 cycles with a capacity retention of 96%. It significantly outperforms the performance in the organic system, which shows a gradual capacity decline with 78% retention after 1000 cycles (Figure 1e). The gradual capacity decline in organic electrolyte can be attributed to the dissolution of active materials during continuous cycling (Figure S7). In addition, the electrochemical performance of PTCDI under a higher mass loading of 2.9 mg is also explored, which provides a superior rate capability (62 mAh g^{-1} at 5 A g^{-1}) and cycle stability (Figure S8). The thermal stability of aqueous electrolyte is demonstrated by thermogravimetry analysis (Figure S9), where the mass loss during heating process mainly associated with the water evaporation. Moreover, the stability of the electrolyte at a low temperature is proved by ionic conductivity and freeze measurement, which still provides a decent ionic conductivity (3.0 mS cm^{-1}) at −15 °C (Figure S10). As a result, PTCDI anode provides comparable capacities at 0 °C and 60 °C as that at room temperature (Figure S11) because of the excellent kinetics. Even at a low temperature of −15 °C, it can still provide a capacity of 94 mAh g^{-1} at 0.1 A g^{-1} (Figure S12).

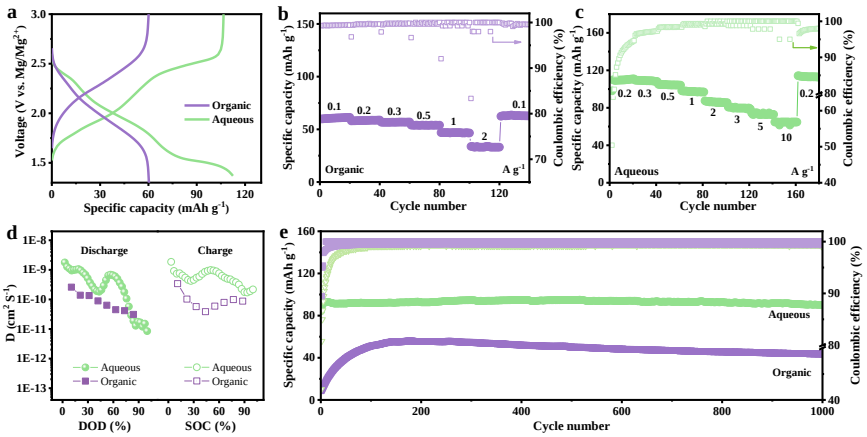

Figure 1. Electrochemical performance of PTCDI in MIBs. a) Voltage profiles in 1 M $Mg(TFSI)_2$-H_2O and 1 M $Mg(TFSI)_2$-EC/PC electrolytes. b) Rate performance in organic electrolyte. The cell is pre-cycled at 0.1 A g^{-1} for 100 cycles to fully activate the electrode for fairly comparing the rate capability. c) Rate performance in aqueous electrolyte without activation. d) Charger diffusivity and e) cyclic performance in organic and aqueous electrolytes at 1 A g^{-1}.

3.2 Synergetic H^+/Mg^{2+} co-storage mechanism and kinetics

Knowing PTCDI anode exhibits totally distinct electrochemical behavior and performance in the two electrolytes, we then explore the underlying mechanisms. For an aqueous system, protons can act as potential charge carriers due to their small size.[44, 45, 49] It is conjectured that the extra redox peaks of PTCDI anode originate from H^+ insertion in aqueous electrolyte. We collect the CV curves of PTCDI anode in the acid electrolyte (i.e., 0.1 M HTFSI in H_2O), without the presence of Mg^{2+}, to examine whether the H^+ insertion exists. As shown in Figure 2a, three reduction peaks at 0.06, −0.37 and −0.64 V vs. Ag/AgCl are obtained in the HTFSI solution, proving the capability of storing H^+ in PTCDI. Based on the Nernst equation, the CV curve in

a pH=6.1 solution (the same pH value with 1 M $Mg(TFSI)_2$-H_2O) is obtained by shifting −0.3 V of the curve in HTFSI solution (Equation S1-S4). The peak positions after shifting can partially overlap with the reduction peaks in $Mg(TFSI)_2$-H_2O electrolyte, suggesting the H^+ insertion in the PTCDI. PTCDI can deliver only a part of capacity in acid solution, attributing to the limited electrochemical window of acid electrolytes (Figure S13).[62, 63] The hydrogen evolution reaction (HER) potential of $Mg(TFSI)_2$-H_2O electrolyte is evaluated to be −1.13 V vs. Ag/AgCl (Figure S14). H^+ insertion is further explored by ^1H solid-state NMR of the PTCDI anode at different states in 1 M $Mg(TFSI)_2$-H_2O (Figure 2b). After discharging to −0.45 V (B point in Figure 2c), an additional weak peak at 4.2 ppm appears, indicating the insertion of H^+ into PTCDI at the early stage of the discharge process. The amount of H^+ increases after full discharge, as confirmed by the enhanced intensity of this peak.[64, 65]

Besides H^+ insertion in PTCDI, Mg^{2+} also involve in the charge storage process, as observed in Mg 1s XPS spectra under different states (Figure 2f). Mg signals gradually appear during the discharge process and almost vanish after full charge. In addition, we examine the Mg^{2+} content in the sample under different states by ICP-OES, which is used to calculate the capacity contribution from Mg^{2+} (Table S1). Under the discharge voltage of −0.45 V vs. Ag/AgCl, Mg^{2+} insertion provides a capacity of 23 mAh g^{-1}, corresponding to 92% of the total capacity (Figure 2d), revealing a Mg^{2+}-dominated storage process accompanied by a small amount of H^+ insertion. As discharging proceeds to −0.9 V, the Mg^{2+} content increases, but its contribution reduces to 68% because of increased H^+ storage. At the fully discharge state, the capacity provided by

H^+ is around 43 mAh g^{-1}, accounting for the capacity difference in the organic and aqueous electrolytes. These results are consistent with the Mg content per PTCDI obtained from elemental mappings (Figure S15 and Table S2). The above observations demonstrate simultaneous Mg^{2+} and H^+ insertion in the PTCDI anode under aqueous electrolyte, where H^+ storage contributes around 40% of the total capacity. The inserted protons may generate from electrolyte with weak acidic property and water dissociation in this system. The dissociation barrier for H_2O on the surface of PTCDI (0.77 eV) is lower than that in vacuum state (6.91 eV), suggesting the possibility of the dissociation during discharge.

The reaction mechanisms of PTCDI during cycling are probed by ex-situ FTIR and XPS under selected states. Figure 2g illustrates the O 1s XPS spectrum of pristine PTCDI, demonstrating the presence of C=O peak at 531.8 eV (Figure 2h). During discharging, the intensity of C=O groups gradually weakens, while a new peak at 533.1 eV corresponding to $C\text{-}O^-$ groups appears and becomes more intense, suggesting an enolization reaction of C=O groups. During the subsequent charging process, the peak of $C\text{-}O^-$ almost disappears and the C=O peak recovers to its initial intensity due to the conversion of $C\text{-}O^-$ back to C=O. The observation is further confirmed by FTIR spectra (Figure 2e). During discharge, the stretching vibration of carbonyl group at ~1672 cm^{-1} weakens and a new peak at ~1050 cm^{-1} ($C\text{-}O^-$) is detected.[66, 67] Upon charging, a reverse conversion of $C\text{-}O^-$ to C=O is observed, as evidenced by the increase of C=O vibration at 1672 cm^{-1} and gradual decrease of $C\text{-}O^-$ peak at 1050 cm^{-1}.

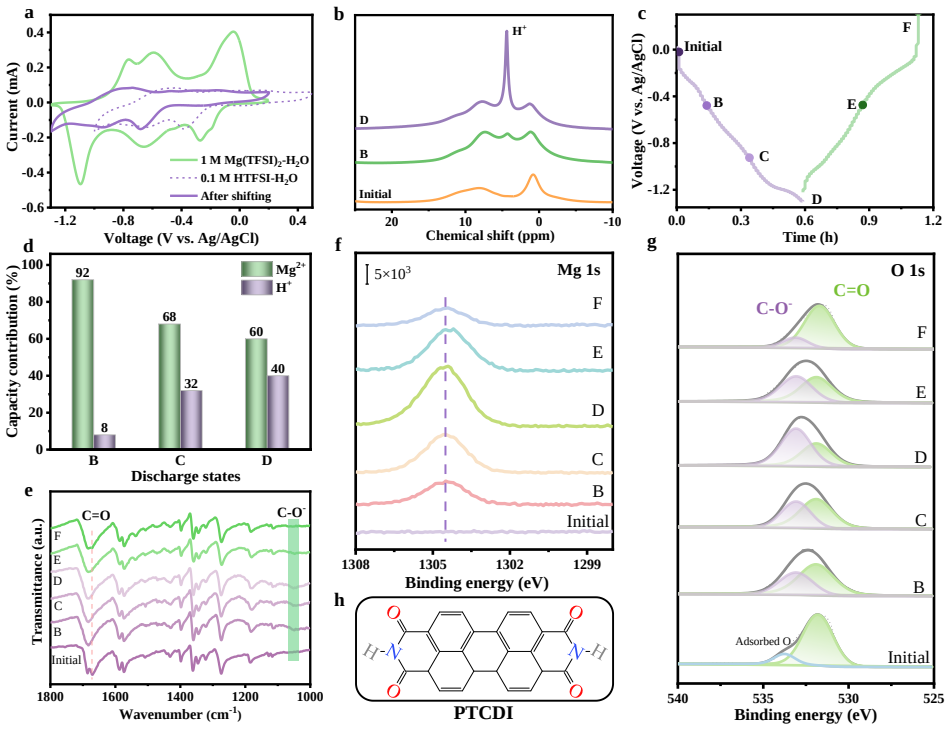

Figure 2. The charge storage mechanism of PTCDI anode. a) CV curves of PTCDI anode in 1 M $Mg(TFSI)_2$-H_2O and 0.1 M HTFSI-H_2O at 1 mV s^{-1}. b) ^1H solid-state NMR spectra of pristine and discharged PTCDI. c) Galvanostatic charge/discharge (GCD) curves under 0.2 A g^{-1}. We mark the charge/discharge states at which the ex-situ FTIR and XPS patterns are collected. d) Calculated H^+/Mg^{2+} capacity contribution at different states. e) Ex-situ FTIR spectra at selected potentials. f) Ex-situ Mg 1s XPS and g) O 1s XPS patterns at selected states. h) Chemical structure of PTCDI.

Density functional theory (DFT) simulations are conducted to further elucidate the H^+/Mg^{2+} storage in PTCDI. Based on the electrostatic interaction, the more negative sites in electrostatic potential (ESP) map stand for the electrophilic centers and are highly active for cations uptake.[68] The ESP map of PTCDI is depicted in Figure 3a. The C=O groups region colored in blue shows the minimal ESP values in PTCDI,

suggesting that C=O bonds are potential electrophilic centers to store cations (H^+ or Mg^{2+}), which is consistent with the ex-situ FTIR and XPS observations. A systematic investigation is performed to calculate the binding energy (ΔE) of various possible geometrical configurations that uptake H^+ and Mg^{2+} step-by-step (Figure S16-S19). The PTCDI incorporates one Mg^{2+} initially with the strongest binding strength of −2.95 eV in the two-electron reaction. It absorbs two H^+ in the subsequent reaction with ΔE values of −3.64 eV and −3.59 eV, respectively. The ΔE of H^+ insertion is reduced after Mg^{2+} insertion into PTCDI, indicating the synergetic effect between them. It is concluded that PTCDI demonstrates a mixed H^+/Mg^{2+}-insertion process and results in the optimized insertion configuration in Figure 3b. The charge density difference distributions of inserted ions (single Mg^{2+} and H^+/Mg^{2+}) at the most favorable insertion site are discussed to further understand the insertion mechanism. As shown in Figure 3c, the O-H and O-Mg bonds exhibit obviously charge transfer to the neighbor O-C bonds in PTCDI, indicating the strong interaction of H^+ and Mg^{2+} with the PTCDI. The investigation of Mg^{2+} diffusion is a crucial task as it is closely linked to the rate capability of batteries. The climbing image nudged elastic band (CI-NEB) method is employed to investigate the pathway of Mg^{2+} from one energetically most favorable insertion site to a neighboring stable site within the PTCDI crystal. As illustrated in Figure 3d, the energy barriers associated with Mg^{2+} diffusion is approximately 0.78 eV, whereas the co-insertion of H^+ can lower the energy barrier to 0.61 eV, thereby facilitating the diffusion of Mg^{2+} in the system. Figure 3e depicts the working mechanism of H^+ co-insertion to enhance the electrochemical performance of PTCDI

anode. In non-aqueous electrolyte, pure Mg^{2+} storage shows characteristics of low capacity, poor rate capability and long activation process owing to limited utilization of active groups and sluggish diffusion kinetics. By contrast, the presence of H^+ co-insertion in the aqueous system brings about two benefits: i) rapid diffusion kinetics for superior rate capability; ii) a 40% capacity improvement by H^+ coordination with un-utilized active sites. It is a delight to find that the H^+ insertion could contribute additional capacity while does not deteriorate the Mg^{2+} storage.

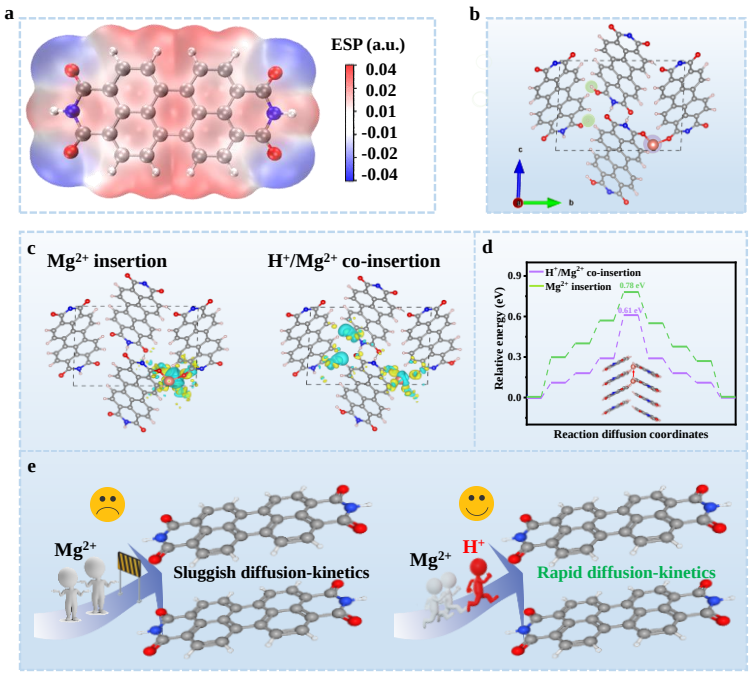

Figure 3. Theoretical simulations of PTCDI anode. a) Calculated ESP map of PTCDI. b) Preferable H^+/Mg^{2+}-PTCDI insertion structure. c) The charge density difference distributions after Mg^{2+} and H^+/Mg^{2+} insertion into the PTCDI, respectively. d) The diffusion energy barriers of Mg^{2+} in PTCDI and H^+ co-inserted PTCDI. Inset shows the diffusion pathway of Mg^{2+} confined within the channel of PTCDI. The C, N, H, O and Mg atoms are represented in grey, blue, pink, red and orange, respectively. e) Schematic diagram of single Mg^{2+} and synergetic Mg^{2+} and H^+ diffusion in PTCDI anode.

3.3 Construction of an aqueous full cell

To demonstrate the practical application of PTCDI in aqueous system, a full battery is fabricated by coupling with a Mg_xCuHCF cathode. Mg_xCuHCF is prepared by electrochemical magnesiation of CuHCF, which is synthesized by a facile co-precipitation method.[69] The Mg signals in elemental mappings and XPS spectrum of magnesiated CuHCF demonstrate the Mg^{2+} insertion (Figure S20 and 21). We first evaluate the performance of Mg_xCuHCF in aqueous MIBs. As shown in Figure S22, the capacity of Mg_xCuHCF decreases rapidly from 50 to 11 mAh g^{-1} after 500 cycles in 1 M $Mg(TFSI)_2$-H_2O electrolyte due to the dissolution of metal ions.[69] This can be suppressed by increasing the electrolyte concentration to 3 M. PTCDI anode shows a similar voltage profile and comparable capacity in 3 M aqueous electrolyte with that in 1 M one (Figure S23); thus the full cell is fabricated in 3 M aqueous electrolyte. According to the CV curves of PTCDI anode and Mg_xCuHCF cathode, the full cell is charged/discharged between 0-2.3 V (Figure 4b). The assembled battery delivers a specific capacity of 96 mAh g^{-1} with an output voltage of ~1.1 V (Figure 4c). Specific capacities of 89, 86, 84, 83, 79, 73 and 72 mAh g^{-1} are achieved at 0.5, 1, 2, 3, 5, 8 and 10 A g^{-1}, respectively, exhibiting a remarkable rate capability (Figure 4c and d). In addition, the full cell can also perform well at low temperatures, which provides 77 and 54 mAh g^{-1} at 0 and −15 ^{o}C, respectively (Figure 4e). Figure 4f shows the comparison of this system with other reported aqueous MIBs, demonstrating competitive rate capability. Lastly, the full cell can stably run for 2000 cycles at 1 A g^{-1}, verifying long-term cyclic stability (Figure 4g).

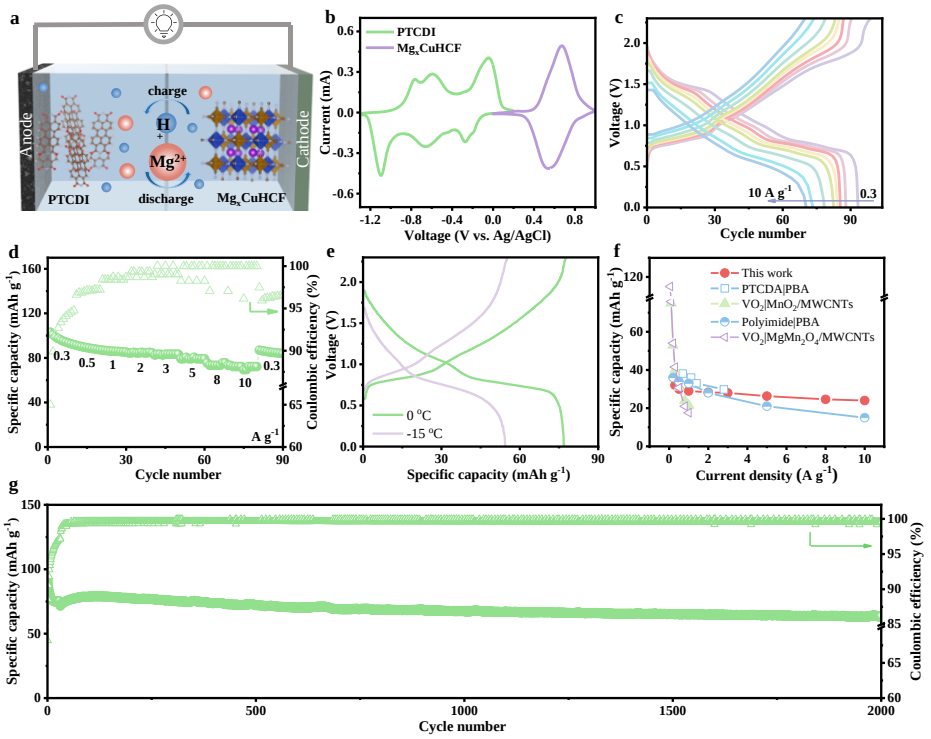

Figure 4. Aqueous Mg ion full cell based on PTCDI anode. a) Schematic diagram of the PTCDI|Mg$_x$CuHCF full cell. b) CV curves of PTCDI anode and Mg$_x$CuHCF cathode. c) Voltage profiles and d) rate performance at a series of current densities. e) Voltage profiles at 0 °C and −15 °C under 0.3 A g^{-1}. f) Rate performance comparison with other reported aqueous MIBs.[11, 70-72] g) Long-term cyclic stability at 1 A g^{-1} after cycling at 0.3 A g^{-1} for 30 cycles. The current densities and specific capacities in Figure 4c, d, e and g are calculated based on the mass of PTCDI anode. Capacities in Figure 4f are calculated based on the total mass of anode and cathode.

3.4 Exploration in Ca-ion system

We further extend the exploration to CIBs to investigate whether the H^+ co-insertion presents and the effect on Ca^{2+} storage. The voltage of AC electrode in Ca-based systems are calibrated according to previous report.[51] As shown in Figure 5a,

it exhibits a similar phenomenon to that in MIBs: PTCDI delivers a much higher specific capacity in aqueous electrolyte than that in organic one, with different voltage plateaus. In addition, PTCDI also delivers a superior rate capability and higher ionic diffusion coefficient in aqueous system than that in organic one (Figure S24-26). The CV curves in HTFSI-H_2O are collected to identify the protons storage in aqueous electrolyte. For a clear comparison, we down-shift the curve in HTFSI-H_2O solution to calibrate the potential caused by the pH difference between it and $Ca(TFSI)_2$-H_2O electrolyte. The location of the reduction peaks overlapped with that in 1 M $Ca(TFSI)_2$-H_2O, endorsing the H^+ storage (Figure 5b). The H^+ insertion could be further confirmed by the characteristic peak in ^1H solid-state NMR spectrum of fully discharged PTCDI (Figure 5c). Strong Ca 2p signal appears in the XPS pattern of discharged PTCDI, which almost vanishes after charge. The observations confirm the reversible Ca^{2+} storage in PTCDI (Figure S27b). The capacity contribution from Ca^{2+} is determined to be 59% according to the Ca^{2+} content in the fully discharged sample measured by the ICP-OES (Inset of Figure 5c and Table S3). Therefore, a 41% capacity (i.e., 46 mAh g^{-1}) is gained from H^+ insertion. Ex-situ FTIR and O 1s XPS reveal the reversible conversion between C=O and C-O^- is responsible for the cation storage (Figure S27a and S28). The H^+/Ca^{2+} insertion pathway and kinetics are further explored by DFT simulations. As shown in Figure S29-31, PTCDI anode undergoes a similar reaction pathway in aqueous CIBs with that in MIBs. The diffusion energy barrier of Ca^{2+} in PTCDI is about 0.81 eV, which decreased to 0.62 eV when the H^+ co-insertion occurs (Figure S32). Therefore, the H^+/Ca^{2+} co-insertion leads to a fast ion diffusion kinetics.

Finally, a PTCDI|Ca_xCuHCF full cell is also assembled to demonstrate the application potential. The cell delivers an average voltage of ~1.1 V, fast charge/discharge capability (66% capacity retention at 10 A g^{-1} vs. that at 0.3 A g^{-1}) and long cyclic life (3000 cycles) (Figure 5d, e and Figure S33). The stabilization process during initial cycles may be ascribed to the existence of residual oxygen during fabrication procedure, which gradually decreases during cycling.[14] The full cell experiences a slight capacity increase during the late cycles, which may be derived from the improved utilization of active materials by the reduced particle size (Figure S34).

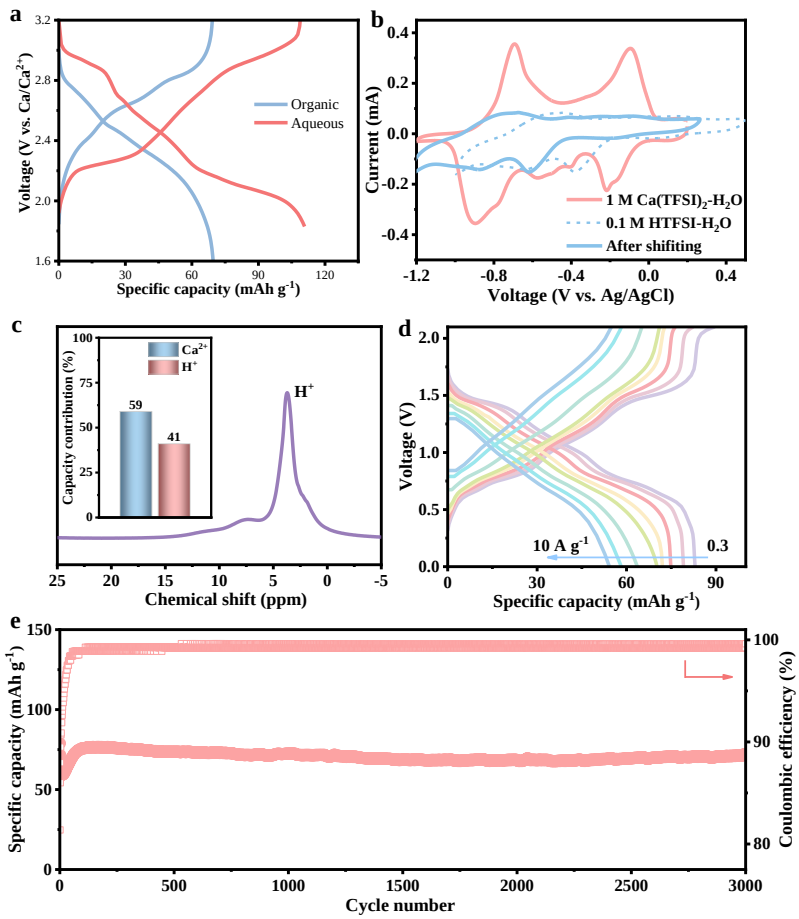

Figure 5. Exploration of PTCDI in Ca-based systems. a) Voltage profiles in 1 M $Ca(TFSI)_2$-H_2O and 1 M $Ca(TFSI)_2$-EC/PC electrolytes. b) CV curves in 1 M $Ca(TFSI)_2$-H_2O and 0.1 M HTFSI-H_2O at 1 mV s^{-1}. c) ^1H solid-state NMR spectrum of fully discharged PTCDI. Inset shows the calculated Ca^{2+} and H^+ capacity contributions. d) GCD curves at various current densities of the full cell. e) Cyclic stability at 1 A g^{-1} of the full cell.

4. Conclusion

In summary, we report a synergetic H^+ and Mg^{2+} storage enabling the advanced organic anode in aqueous MIBs. The co-insertion mechanism leads to a higher specific capacity of 110 mAh g^{-1} in aqueous electrolyte than in the organic counterpart, where

Mg^{2+} acts as the only charge carrier. Furthermore, the proton insertion also benefits the diffusion kinetics to enable fast charging/discharging competence, as proved by electrochemical analysis and DFT calculations. By coupling with a Prussian blue analogue cathode, a high-safety aqueous full cell is demonstrated, which shows remarkable rate performance (72 mAh g^{-1} at 10 A g^{-1}), long-term cyclic stability (2000 cycles) and low-temperature operation capability (−15 ºC), standing out among reported aqueous MIBs. Furthermore, this phenomenon can be extended to the Ca-based system, providing a high-rate and ultra-stable organic anode for aqueous CIBs. This work offers an alternative way to develop high-performance aqueous divalent ion batteries taking advantage of H^+ co-insertion behavior.

References

[1] Y. Liang, H. Dong, D. Aurbach, Y. Yao, Current status and future directions of multivalent metal-ion batteries, Nat. Energy 5 (9) (2020) 646-656, https://doi.org/10.1038/s41560-020-0655-0.

[2] T.T. Liu, X. Cheng, H.X. Yu, H.J. Zhu, N. Peng, R.T. Zheng, J.D. Zhang, M. Shui, Y.H. Cui, J. Shu, An overview and future perspectives of aqueous rechargeable polyvalent ion batteries, Energy Storage Mater. 18 (2019) 68-91, https://doi.org/10.1016/j.ensm.2018.09.027.

[3] A. Ponrouch, M.R. Palacin, On the road toward calcium-based batteries, Curr. Opin. Electrochem. 9 (2018) 1-7, https://doi.org/10.1016/j.coelec.2018.02.001.

[4] J. Xie, Q. Zhang, Recent progress in multivalent metal (Mg, Zn, Ca, and Al) and metal-ion rechargeable batteries with organic materials as promising electrodes, Small

15 (15) (2019) 1805061, https://doi.org/10.1002/smll.201805061.

[5] Z. Zhao-Karger, M.E. Gil Bardaji, O. Fuhr, M. Fichtner, A new class of non-corrosive, highly efficient electrolytes for rechargeable magnesium batteries, J. Mater. Chem. A 5 (22) (2017) 10815-10820, https://doi.org/10.1039/c7ta02237a.

[6] P. Saha, M.K. Datta, O.I. Velikokhatnyi, A. Manivannan, D. Alman, P.N. Kumta, Rechargeable magnesium battery: Current status and key challenges for the future, Prog. Mater. Sci. 66 (2014) 1-86, https://doi.org/10.1016/j.pmatsci.2014.04.001.

[7] L.R. Parent, Y. Cheng, P.V. Sushko, Y. Shao, J. Liu, C.M. Wang, N.D. Browning, Realizing the full potential of insertion anodes for Mg-ion batteries through the nanostructuring of Sn, Nano Lett. 15 (2) (2015) 1177-82, https://doi.org/10.1021/nl5042534.

[8] X. Zhang, R. Lv, W. Tang, G. Li, A. Wang, A. Dong, X. Liu, J. Luo, Challenges and opportunities for multivalent metal anodes in rechargeable batteries, Adv. Funct. Mater. 30 (45) (2020) 2004187, https://doi.org/10.1002/adfm.202004187.

[9] L. Zhou, L. Liu, Z. Hao, Z. Yan, X.-F. Yu, P.K. Chu, K. Zhang, J. Chen, Opportunities and challenges for aqueous metal-proton batteries, Matter 4 (4) (2021) 1252-1273, https://doi.org/10.1016/j.matt.2021.01.022.

[10] Q. Fu, X. Wu, X. Luo, S. Indris, A. Sarapulova, M. Bauer, Z. Wang, M. Knapp, H. Ehrenberg, Y. Wei, S. Dsoke, High-voltage aqueous Mg-ion batteries enabled by solvation structure reorganization, Adv. Funct. Mater. 32 (16) (2022) 2110674, https://doi.org/10.1002/adfm.202110674.

[11] L. Chen, J.L. Bao, X. Dong, D.G. Truhlar, Y. Wang, C. Wang, Y. Xia, Aqueous Mg-

ion battery based on polyimide anode and prussian blue cathode, ACS Energy Lett. 2 (5) (2017) 1115-1121, https://doi.org/10.1021/acsenergylett.7b00040.

[12] M. Adil, P.K. Dutta, S. Mitra, An aqueous Ca-ion full cell comprising BaHCF cathode and MCMB anode, ChemistrySelect 3 (13) (2018) 3687-3690, https://doi.org/10.1002/slct.201800419.

[13] C.-Y. Du, Z.-H. Zhang, X.-L. Li, R.-J. Luo, C. Ma, J. Bao, J. Zeng, X. Xu, F. Wang, Y.-N. Zhou, Enhancing structural and cycle stability of prussian blue cathode materials for calcium-ion batteries by introducing divalent Fe, Chem. Eng. J. 451 (2023) 138650, https://doi.org/10.1016/j.cej.2022.138650.

[14] S. Gheytani, Y. Liang, F. Wu, Y. Jing, H. Dong, K.K. Rao, X. Chi, F. Fang, Y. Yao, An aqueous Ca-ion battery, Adv. Sci. 4 (12) (2017) 1700465, https://doi.org/10.1002/advs.201700465.

[15] V. Soundharrajan, B. Sambandam, S. Kim, V. Mathew, J. Jo, S. Kim, J. Lee, S. Islam, K. Kim, Y.-K. Sun, J. Kim, Aqueous magnesium zinc hybrid battery: An advanced high-voltage and high-energy $MgMn_2O_4$ cathode, ACS Energy Lett. 3 (8) (2018) 1998-2004, https://doi.org/10.1021/acsenergylett.8b01105.

[16] H. Zhang, K. Ye, X. Huang, X. Wang, K. Cheng, X. Xiao, G. Wang, D. Cao, Preparation of $Mg_{1.1}Mn_6O_{12}\cdot 4.5H_2O$ with nanobelt structure and its application in aqueous magnesium-ion battery, J. Power Sources 338 (2017) 136-144, https://doi.org/10.1016/j.jpowsour.2016.10.078.

[17] T. Sun, H. Du, S. Zheng, Z. Tao, Inverse-spinel Mg_2MnO_4 material as cathode for high-performance aqueous magnesium-ion battery, J. Power Sources 515 (2021)

230643, https://doi.org/10.1016/j.jpowsour.2021.230643.

[18] S. Javadian, S.M.J. Ghavam, N. Dalir, H. Gharibi, Template-based design hollow spheres spinel and reduce graphene oxide composite as a super stable cathode for aqueous Mg-ion battery, Mater. Chem. Phys. 284 (2022) 126050, https://doi.org/10.1016/j.matchemphys.2022.126050.

[19] Y. Zhang, G. Liu, C. Zhang, Q. Chi, T. Zhang, Y. Feng, K. Zhu, Y. Zhang, Q. Chen, D. Cao, Low-cost $MgFe_xMn_{2-x}O_4$ cathode materials for high-performance aqueous rechargeable magnesium-ion batteries, Chem. Eng. J. 392 (2020) 123652, https://doi.org/10.1016/j.cej.2019.123652.

[20] Z.Y. Shi, J.H. Wu, M.Z. Ni, Q.B. Guo, F. Zan, H. Xia, Superior performance of calcium birnessite by electrochemical conversion as cathode for aqueous calcium ion battery, Mater. Res. Bull. 144 (2021) 111475, https://doi.org/10.1016/j.materresbull.2021.111475.

[21] X. Sun, V. Duffort, B.L. Mehdi, N.D. Browning, L.F. Nazar, Investigation of the mechanism of mg insertion in birnessite in nonaqueous and aqueous rechargeable Mg-ion batteries, Chem. Mater. 28 (2) (2016) 534-542, https://doi.org/10.1021/acs.chemmater.5b03983.

[22] F. Wang, X. Fan, T. Gao, W. Sun, Z. Ma, C. Yang, F. Han, K. Xu, C. Wang, High-voltage aqueous magnesium ion batteries, ACS Cent. Sci. 3 (10) (2017) 1121-1128, https://doi.org/10.1021/acscentsci.7b00361.

[23] H. Zhang, D. Cao, X. Bai, High rate performance of aqueous magnesium-ion batteries based on the δ-MnO_2@carbon molecular sieves composite as the cathode and

nanowire VO_2 as the anode, J. Power Sources 444 (2019), https://doi.org/10.1016/j.jpowsour.2019.227299.

[24] Y. Zhao, B. Wang, M. Shi, S. An, L. Zhao, C. Yan, Mg-intercalation engineering of MnO_2 electrode for high-performance aqueous magnesium-ion batteries, Int. J. Miner. Metall. Mater. 29 (11) (2022) 1954-1962, https://doi.org/10.1007/s12613-021-2346-7.

[25] Z.M. Qin, Y. Song, Y.Z. Liu, X.X. Liu, Aqueous calcium-ion storage in amorphous molybdenum oxide, Chem. Eng. J. 451 (2023) 138681, https://doi.org/10.1016/j.cej.2022.138681.

[26] M.S. Chae, J.W. Heo, J. Hyoung, S.T. Hong, Double-sheet vanadium oxide as a cathode material for calcium-ion batteries, ChemNanoMat 6 (7) (2020) 1049-1053, https://doi.org/10.1002/cnma.202000011.

[27] G. Yang, X. Xu, G. Qu, J. Deng, Y. Zhu, C. Fang, O. Fontaine, P. Hiralal, J. Zheng, H. Zhou, An aqueous magnesium-ion battery working at −50 ºC enabled by modulating electrolyte structure, Chem. Eng. J. 455 (2023) 140806, https://doi.org/10.1016/j.cej.2022.140806.

[28] X. Tang, D. Zhou, B. Zhang, S. Wang, P. Li, H. Liu, X. Guo, P. Jaumaux, X. Gao, Y. Fu, C. Wang, C. Wang, G. Wang, A universal strategy towards high-energy aqueous multivalent-ion batteries, Nat. Commun. 12 (1) (2021) 2857, https://doi.org/10.1038/s41467-021-23209-6.

[29] R. Zhou, Z. Hou, Q. Liu, X. Du, J. Huang, B. Zhang, Unlocking the reversible selenium electrode for non-aqueous and aqueous calcium-ion batteries, Adv. Funct.

Mater. 32 (26) (2022) 2200929, https://doi.org/10.1002/adfm.202200929.

[30] H. Zhang, K. Ye, K. Zhu, R. Cang, J. Yan, K. Cheng, G. Wang, D. Cao, High-energy-density aqueous magnesium-ion battery based on a carbon-coated $FeVO_4$ anode and a Mg-OMS-1 cathode, Chem. Eur. J. 23 (67) (2017) 17118-17126, https://doi.org/10.1002/chem.201703806.

[31] Y. Tang, X. Li, H. Lv, W. Wang, Q. Yang, C. Zhi, H. Li, High-energy aqueous magnesium hybrid full batteries enabled by carrier-hosting potential compensation, Angew. Chem. Int. Ed. 60 (10) (2021) 5443-5452, https://doi.org/10.1002/anie.202013315.

[32] L. Li, G. Zhang, X. Deng, J. Hao, X. Zhao, H. Li, C. Han, B. Li, A covalent organic framework for high-rate aqueous calcium-ion batteries, J. Mater. Chem. A 10 (39) (2022) 20827-20836, https://doi.org/10.1039/d2ta05185k.

[33] X.M. Deng, J.K. Sarpong, G.B. Zhang, J. Hao, X. Zhao, L.Y. Li, H.F. Li, C.P. Han, B.H. Li, Proton storage chemistry in aqueous zinc-organic batteries: A review, Infomat 5 (2) (2023) e12382, https://doi.org/10.1002/inf2.12382.

[34] H. Zhang, Y. Gao, X.H. Liu, Z. Yang, X.X. He, L. Li, Y. Qiao, W.H. Chen, R.H. Zeng, Y. Wang, S.L. Chou, Organic cathode materials for sodium-ion batteries: From fundamental research to potential commercial application, Adv. Funct. Mater. 32 (4) (2021) 2107718, https://doi.org/10.1002/adfm.202107718.

[35] Y. Lu, J. Chen, Prospects of organic electrode materials for practical lithium batteries, Nat. Rev. Chem. 4 (3) (2020) 127-142, https://doi.org/10.1038/s41570-020-0160-9.

[36] X. Lei, Y. Zheng, F. Zhang, Y. Wang, Y. Tang, Highly stable magnesium-ion-based dual-ion batteries based on insoluble small-molecule organic anode material, Energy Storage Mater. 30 (2020) 34-41, https://doi.org/10.1016/j.ensm.2020.04.025.

[37] C. Han, H. Li, Y. Li, J. Zhu, C. Zhi, Proton-assisted calcium-ion storage in aromatic organic molecular crystal with coplanar stacked structure, Nat. Commun. 12 (1) (2021) 2400, https://doi.org/10.1038/s41467-021-22698-9.

[38] M.S. Chae, A. Nimkar, N. Shpigel, Y. Gofer, D. Aurbach, High performance aqueous and nonaqueous Ca-ion cathodes based on fused-ring aromatic carbonyl compounds, ACS Energy Lett. 6 (8) (2021) 2659-2665, https://doi.org/10.1021/acsenergylett.1c01010.

[39] L.E. Blanc, X. Sun, A. Shyamsunder, V. Duffort, L.F. Nazar, Direct nano-synthesis methods notably benefit Mg-battery cathode performance, Small Methods 4 (5) (2020) 2000029, https://doi.org/10.1002/smtd.202000029.

[40] L. Jiang, Y. Lu, C. Zhao, L. Liu, J. Zhang, Q. Zhang, X. Shen, J. Zhao, X. Yu, H. Li, X. Huang, L. Chen, Y.-S. Hu, Building aqueous K-ion batteries for energy storage, Nat. Energy 4 (6) (2019) 495-503, https://doi.org/10.1038/s41560-019-0388-0.

[41] L. Yang, P. Wang, S. Zhang, Y. Wang, L. Zang, H. Zhu, J. Yin, H.Y. Yang, Flexible and additive-free organic electrodes for aqueous sodium ion batteries, J. Mater. Chem. A 8 (43) (2020) 22791-22801, https://doi.org/10.1039/d0ta07267b.

[42] X. Wu, Y. Qi, J.J. Hong, Z. Li, A.S. Hernandez, X. Ji, Rocking-chair ammonium-ion battery: A highly reversible aqueous energy storage system, Angew. Chem. Int. Ed. 56 (42) (2017) 13026-13030, https://doi.org/10.1002/anie.201707473.

[43] I.A. Rodriguez-Perez, Y. Yuan, C. Bommier, X. Wang, L. Ma, D.P. Leonard, M.M. Lerner, R.G. Carter, T. Wu, P.A. Greaney, J. Lu, X. Ji, Mg-ion battery electrode: An organic solid's herringbone structure squeezed upon Mg-ion insertion, J. Am. Chem. Soc. 139 (37) (2017) 13031-13037, https://doi.org/10.1021/jacs.7b06313.

[44] K. Zhu, T. Wu, S. Sun, W. van den Bergh, M. Stefik, K. Huang, Synergistic H^+/Zn^{2+} dual ion insertion mechanism in high-capacity and ultra-stable hydrated VO_2 cathode for aqueous Zn-ion batteries, Energy Storage Mater. 29 (2020) 60-70, https://doi.org/10.1016/j.ensm.2020.03.030.

[45] Z. Tie, L. Liu, S. Deng, D. Zhao, Z. Niu, Proton insertion chemistry of a zinc-organic battery, Angew. Chem. Int. Ed. 59 (12) (2020) 4920-4924, https://doi.org/10.1002/anie.201916529.

[46] Y. Zhang, C. Zhao, Z. Li, Y. Wang, L. Yan, J. Ma, Y. Wang, Synergistic co-reaction of Zn^{2+} and H^+ with carbonyl groups towards stable aqueous zinc-organic batteries, Energy Storage Mater. 52 (2022) 386-394, https://doi.org/10.1016/j.ensm.2022.08.005.

[47] M. Na, Y. Oh, H.R. Byon, Effects of Zn^{2+} and H^+ association with naphthalene diimide electrodes for aqueous Zn-ion batteries, Chem. Mater. 32 (16) (2020) 6990-6997, https://doi.org/10.1021/acs.chemmater.0c02357.

[48] W. Sun, F. Wang, S. Hou, C. Yang, X. Fan, Z. Ma, T. Gao, F. Han, R. Hu, M. Zhu, C. Wang, Zn/MnO_2 battery chemistry with H^+ and Zn^{2+} coinsertion, J. Am. Chem. Soc. 139 (29) (2017) 9775-9778, https://doi.org/10.1021/jacs.7b04471.

[49] S. Wang, Z. Yuan, X. Zhang, S. Bi, Z. Zhou, J. Tian, Q. Zhang, Z. Niu, Non-metal ion co-insertion chemistry in aqueous Zn/MnO_2 batteries, Angew. Chem. Int. Ed. 60

(13) (2021) 7056-7060, https://doi.org/10.1002/anie.202017098.

[50] Z. Liu, X. Li, J. He, Q. Wang, D. Zhu, Y. Yan, Y. Chen, Is proton a charge carrier for δ-MnO_2 cathode in aqueous rechargeable magnesium-ion batteries?, J. Energy Chem. 68 (2022) 572-579, https://doi.org/10.1016/j.jechem.2021.12.016.

[51] R. Zhou, Z. Hou, K. Fan, C.K. Wun, Q. Liu, T.W. Benedict Lo, H. Huang, B. Zhang, An advanced organic cathode for non-aqueous and aqueous calcium-based dual ion batteries, J. Power Sources 569 (2023) 232995, https://doi.org/10.1016/j.jpowsour.2023.232995.

[52] Z. Zhang, Y. Li, G. Zhao, L. Zhu, Y. Sun, F. Besenbacher, M. Yu, Rechargeable Mg-ion full battery system with high capacity and high rate, ACS Appl. Mater. Interfaces 13 (34) (2021) 40451-40459, https://doi.org/10.1021/acsami.1c06106.

[53] R. Li, J. Yu, F. Chen, Y. Su, K.C. Chan, Z.-L. Xu, High-power and ultrastable aqueous calcium-ion batteries enabled by small organic molecular crystal anodes, Adv. Funct. Mater. 33 (30) (2023) 2214304, https://doi.org/10.1002/adfm.202214304.

[54] Z. Hou, R. Zhou, Y. Yao, Z. Min, Z. Lu, Y. Zhu, J.-M. Tarascon, B. Zhang, Correlation between electrolyte chemistry and solid electrolyte interphase for reversible Ca metal anodes, Angew. Chem. Int. Ed. 61 (50) (2022) e202214796, https://doi.org/10.1002/anie.202214796.

[55] M. Rastgoo-Deylami, M.S. Chae, S.-T. Hong, $H_2V_3O_8$ as a high energy cathode material for nonaqueous magnesium-ion batteries, Chem. Mater. 30 (21) (2018) 7464-7472, https://doi.org/10.1021/acs.chemmater.8b01381.

[56] Y. Chen, K. Fan, Y. Gao, C. Wang, Challenges and perspectives of organic

multivalent metal-ion batteries, Adv. Mater. 34 (52) (2022) 2200662, https://doi.org/10.1002/adma.202200662.

[57] Y. Ding, D. Chen, X. Ren, Y. Cao, F. Xu, Organic-conjugated polyanthraquinonylimide cathodes for rechargeable magnesium batteries, J. Mater. Chem. A 10 (26) (2022) 14111-14120, https://doi.org/10.1039/d2ta02795j.

[58] X.Z. Zhai, J. Qu, S.M. Hao, Y.Q. Jing, W. Chang, J. Wang, W. Li, Y. Abdelkrim, H. Yuan, Z.Z. Yu, Layered birnessite cathode with a displacement/intercalation mechanism for high-performance aqueous zinc-ion batteries, Nano-micro Lett. 12 (1) (2020) 56, https://doi.org/10.1007/s40820-020-0397-3.

[59] W. Weppner, R.A. Huggins, Determination of the kinetic parameters of mixed-conducting electrodes and application to the system Li_3Sb, J. Electrochem. Soc. 124 (10) (1977) 1569, https://doi.org/10.1149/1.2133112.

[60] W. Tang, Y.S. Zhu, Y.Y. Hou, L.L. Liu, Y.P. Wu, K.P. Loh, H.P. Zhang, K. Zhu, Aqueous rechargeable lithium batteries as an energy storage system of superfast charging, Energy. Environ. Sci. 6 (7) (2013) 2093-2104, https://doi.org/10.1039/c3ee24249h.

[61] Y. Wang, J. Yi, Y.J.A.E.M. Xia, Recent progress in aqueous lithium-ion batteries, Adv. Energy Mater. 2 (7) (2012) 830-840, https://doi.org/10.1002/aenm.201200065.

[62] X. Liu, H. Euchner, M. Zarrabeitia, X. Gao, G.A. Elia, A. Gross, S. Passerini, Operando pH measurements decipher H^+/Zn^{2+} intercalation chemistry in high-performance aqueous Zn/δ-V_2O_5 batteries, ACS Energy Lett. 5 (9) (2020) 2979-2986, https://doi.org/10.1021/acsenergylett.0c01767.

[63] J. Fortunato, Y.K. Shin, M.A. Spencer, A.C.T. van Duin, V. Augustyn, Choice of electrolyte impacts the selectivity of proton-coupled electrochemical reactions on hydrogen titanate, J. Phys. Chem. C 127 (25) (2023) 11810-11821, https://doi.org/10.1021/acs.jpcc.3c01057.

[64] X. Chen, X. Hu, Y. Chen, X. Cao, Y. Huang, H. Zhang, J.-H. Liu, Y. Wang, S.-L. Chou, D. Cao, Ultrastable hydrated vanadium dioxide cathodes for high-performance aqueous zinc ion batteries with H^+/Zn^{2+} co-insertion mechanism, J. Mater. Chem. A 10 (41) (2022) 22194-22204, https://doi.org/10.1039/d2ta07101k..

[65] X. Wang, Y. Liu, Z. Wei, J. Hong, H. Liang, M. Song, Y. Zhou, X. Huang, Mxene-boosted imine cathodes with extended conjugated structure for aqueous zinc-ion batteries, Adv. Mater. 34 (50) (2022) 2206812, https://doi.org/10.1002/adma.202206812.

[66] X. Zheng, W. Wang, T. Huang, G. Fang, Y. Pan, M. Wu, Evaluation of di(2,2,2-trifluoroethyl) sulfite as a film-forming additive on the mcmb anode of lithium-ion batteries, J. Power Sources 329 (2016) 450-455, https://doi.org/10.1016/j.jpowsour.2016.08.108.

[67] Z. Qiu, C. Liu, J. Xin, Q. Wang, J. Wu, W. Wang, J. Zhou, Y. Liu, B. Guo, S. Shi, High conductive composite polymer electrolyte via in situ UV-curing for all-solid-state lithium ion batteries, ACS Sustain. Chem. Eng. 7 (11) (2019) 9875-9880, https://doi.org/10.1021/acssuschemeng.9b00474.

[68] F. Yue, Z. Tie, S. Deng, S. Wang, M. Yang, Z. Niu, An ultralow temperature aqueous battery with proton chemistry, Angew. Chem. Int. Ed. 60 (25) (2021) 13882-

13886, https://doi.org/10.1002/anie.202103722.

[69] C. Lee, S.-K. Jeong, Modulating the hydration number of calcium ions by varying the electrolyte concentration: Electrochemical performance in a prussian blue electrode/aqueous electrolyte system for calcium-ion batteries, Electrochim. Acta 265 (2018) 430-436, https://doi.org/10.1016/j.electacta.2018.01.172.

[70] D. Zhang, D. Du, J. Zhang, Z. Feng, T. Sun, Porous spinel magnesium manganese oxide/multiwalled carbon nanotubes composite synthesized by electrochemical conversion as high-performance cathode for aqueous magnesium ion battery, J. Electrochem. Soc. 169 (4) (2022), https://doi.org/10.1149/1945-7111/ac6451.

[71] D. Zhang, W. Huang, T. Chen, Q. Wang, T. Sun, Facile synthesis of MnO_2/MWCNTs via UV photolysis as high-performance and low-cost cathodes for aqueous magnesium ion batteries, ACS Appl. Energy Mater. 4 (7) (2021) 6853-6865, https://doi.org/10.1021/acsaem.1c00971.

[72] Y. Zhu, X. Guo, Y. Lei, W. Wang, A.-H. Emwas, Y. Yuan, Y. He, H.N. Alshareef, Hydrated eutectic electrolytes for high-performance Mg-ion batteries, Energy. Environ. Sci. 15 (3) (2022) 1282-1292, https://doi.org/10.1039/d1ee03691b.